scientific reports

Check for updates

OPEN

Full-process deformation monitoring and failure characteristics analysis of damaged coal under 3D laser scanning technology

Peihua Jiang[1], Yang Liu[1,2]✉ & Guangke Li[3]

During underground coal mining, coal bodies are highly susceptible to deformation and damage under repeated excavation-induced disturbances, which significantly increases the risk of dynamic coal-rock disasters. To investigate the deformation and failure characteristics of coal under repeated excavation-induced disturbances and to improve disaster prevention and control capabilities, quasi-static uniaxial cyclic loading-unloading (L-U) tests, as well as dynamic axial compression tests under impact loading, were conducted on large-scale coal-like specimens. During the tests, three-dimensional (3D) laser scanning technology and high-precision total station measurements were employed to accurately capture the deformation data of the specimens at each testing stage. This enabled a systematic analysis of the deformation and failure evolution. Results indicate that: (1) During the quasi-static uniaxial cyclic L-U process, the maximum loading stress is the most critical factor affecting the deformation. With increasing cycle numbers, the specimens loaded to the yield stage exhibit progressively increasing deformation; those specimens loaded to the elastic stage show a trend of initial decrease followed by an increase; while specimens loaded to the compaction stage demonstrate a continuous decrease in deformation. (2) Acoustic emission (AE) monitoring results revealed a damage evolution mechanism characterized by the alternating dominance of crack compaction and propagation during cyclic loading. The damage contribution rate rose with both loading intensity and cycle number, showing that early-stage damage accumulation provided the basis for later dynamic failure. (3) After the application of dynamic impact loading, all specimens failed mainly by splitting failure. Specimens with lower levels of pre-existing damage experienced more severe failure, indicating that greater energy was accumulated during the preceding cyclic L-U process. (4) The deformation evolution patterns obtained by the 3D laser scanning technique were highly consistent with the axial displacement curves measured by the total station, with the maximum deviation less than 2.5%, which meets the permissible error requirements of laboratory testing. This direct comparison confirms the accuracy and reliability of the scanning data. Furthermore, the 3D laser scanning method demonstrates higher operational efficiency in field applications, highlighting its strong engineering applicability and potential for broader adoption.

Keywords 3D laser scanning, Quasi-static uniaxial cyclic loading-unloading, Dynamic impact loading, Deformation evolution, Failure characteristics

With the accelerated pace of global industrialization and the continuous growth in energy demand, coal, as a vital fundamental energy resource, has been extensively mined and utilized[1,2]. However, during actual underground coal mining operations, frequent excavation activities induce cyclic loading-unloading (L-U) effects that significantly alter the physical and mechanical properties of the coal and rock mass. These changes can lead to deformation and fracturing of the coal and rock mass, which, under dynamic disturbances such as roof collapses, may further trigger severe mine dynamic disasters[3–5]. In recent years, numerous researchers have

[1]School of Architecture Engineering, North China Institute of Science and Technology, Langfang 065201, China. [2]Shanxi Technology and Business University, Taiyuan 030062, China. [3]Shandong Tianyu Construction Engineering Co., LTD, Zibo 255200, China. ✉email: liuyang940131@163.com

systematically investigated the mechanical response characteristics of coal and rock masses under combined static and dynamic loading conditions through laboratory experiments and numerical simulations[6–9], as well as the evolution patterns of their deformation and failure behaviors[10–12]. Additionally, the damage and failure mechanisms have been explored from perspectives such as stress wave propagation and energy dissipation characteristics. With the continuous increase in mining depth and intensity, the deformation and instability processes of coal have become increasingly complex. Traditional monitoring methods, due to limitations such as a small number of observation points, discontinuous data acquisition, and complex operation procedures, are insufficient to comprehensively and accurately capture the true deformation behavior of coal[13].

As a rapidly developing technology for acquiring three-dimensional (3D) spatial data, 3D laser scanning offers significant advantages such as non-contact measurement, high accuracy, fast data acquisition, and the ability to achieve realistic scene reconstruction. It has been widely applied in various fields, including construction engineering surveying[14–16], road surface and terrain monitoring[17], cultural heritage preservation[18], and disaster monitoring[16]. In the field of mining engineering, Zhang et al.[19] analyzed the feasibility of applying 3D laser scanning technology to monitor ground subsidence induced by mining activities, based on the technical characteristics of the scanning system. Kajzar et al.[20] employed this technology to monitor coal pillar deformation and roof movement, achieving promising results. Huang et al.[21] effectively characterized the overall deformation state of roadway supports based on point cloud data acquired through 3D laser scanning, providing an efficient and reliable monitoring method to enhance roadway support safety. However, current research on monitoring the deformation evolution characteristics of disturbed coal under cyclic L-U remains relatively limited, highlighting the urgent need to further explore the application potential of this technology in full-process monitoring of coal deformation and damage.

In this study, 3D laser scanning technology is employed to overcome the limitations of traditional single-point measurement methods, enabling comprehensive monitoring of the deformation and failure behavior of damaged coal specimens during testing. By rapidly acquiring the 3D morphological data of the specimens, this approach significantly enhances the accuracy and efficiency of deformation monitoring, providing more reliable data support for in-depth analysis of the deformation evolution of coal. The application of this technology can provide a scientific basis for safety management and mining design in coal resource extraction, contributing to the reduction of mine disaster risks. It holds significant importance for achieving safe, efficient, and sustainable coal mining.

Test design

Specimens preparation

To closely replicate the stress and deformation characteristics of coal during actual mining operations and to overcome the limitations of conventional laboratory specimen sizes, large cubic specimens with a side length of 450 mm were adopted in this study, in accordance with the capabilities of the 15 MN large-scale dynamic material testing machine. As it is extremely difficult to obtain large-size specimens directly from coal mines, and the inherent heterogeneity of natural coal may lead to significant variability in test results, coal-like specimens were fabricated using a casting method with similar materials.

Based on a review of relevant literature[22], Portland cement, coal powder, water, water-reducing agent, and retarder were selected as the constituent materials for preparing the coal-like specimens. By adjusting the mass ratio of cement to coal powder, the physical and mechanical properties of the specimens were controlled. The water-reducing agent was used to improve the workability of the mixture and reduce the water demand, while the retarder was employed to slow down the hydration rate and heat release of the cement, thereby minimizing the internal and external temperature differences of the specimens and preventing surface cracking during the initial setting process. A total of 12 mix proportion schemes were designed for this test. Standard-sized cylindrical coal-like specimens (Diameter ø=50 mm, Height H = 100 mm) were prepared accordingly, and their fundamental physical and mechanical properties were tested. The test results of each group of mix-proportioned specimens were compared with the corresponding parameters of standard-sized raw coal specimens, the physical and mechanical properties of the raw coal specimens as shown in Table 1. The results are presented in Table 2. It was found that the mechanical properties of the P_4 scheme were the closest to those of the raw coal specimens. In this scheme, the mass ratio of cement to coal powder was 7:3, the dosage of the water reducer was 0.25% of the cement mass, the dosage of the retarder was 0.2% of the cement mass, and the water-to-cement ratio was 0.45.

The comparison of laboratory-determined mechanical property curves between the standard-sized coal-like specimens prepared using the P_4 scheme and the raw coal specimens is shown in Fig. 1, further verifying the feasibility and representativeness of the selected scheme. Based on these results, the P_4 scheme was ultimately adopted for the preparation of large-scale coal-like specimens with dimensions of 450 mm.

Loading and unloading scheme

This test aims to investigate the deformation and failure characteristics of coal subjected to multiple excavation-induced disturbances and subsequent impact dynamic loading. Considering the cumulative disturbance effects induced by repeated mining activities on the deformation behavior of deep coal masses, the historical maximum stress experienced by the coal during actual excavation is represented in the test as the maximum loading stress

Densityρ/(kg m^{-3})	Uniaxial compressive strength σ_0/MPa	Elastic modulusE/GPa	Poisson's ratiov
1349	17.761	2.012	0.259

Table 1. Physical and mechanical properties of the Raw coal specimen.

Scheme	Density ρ/(kg m^{-3})		Uniaxial compressive strength σ_0/MPa		Elastic modulus E/GPa		Poisson's ratio ν	
	Measured value	Relative error(%)	Measured value	Relative error(%)	Measured value	Relative error(%)	Measured value	Relative error(%)
P_1	1304	− 3.34	12.190	− 31.37	1.339	− 33.45	0.290	11.97
P_2	1317	− 2.37	16.365	− 7.86	1.939	− 3.63	0.275	6.18
P_3	1328	− 1.56	10.366	− 41.64	1.538	− 23.56	0.294	13.51
P_4	1359	0.74	17.490	− 1.53	2.319	15.26	0.205	− 20.85
P_5	1313	− 2.67	10.448	− 41.17	1.596	− 20.68	0.285	10.04
P_6	1338	− 0.82	13.017	− 26.71	1.812	− 9.94	0.348	34.36
P_7	1297	− 3.85	4.644	− 73.85	1.360	− 32.41	0.341	31.66
P_8	1305	− 3.26	15.799	− 11.05	1.860	− 7.55	0.283	9.27
P_9	1361	0.89	4.357	− 75.47	1.244	− 38.17	0.372	43.63
P_{10}	1325	− 1.78	6.672	− 62.43	1.431	− 28.88	0.344	32.82
P_{11}	1336	− 0.96	2.690	− 84.85	0.881	− 56.21	0.415	60.23
P_{12}	1381	2.37	7.063	− 60.23	1.533	− 23.81	0.325	25.48

Table 2. Physical and mechanical properties of the coal-like specimens.

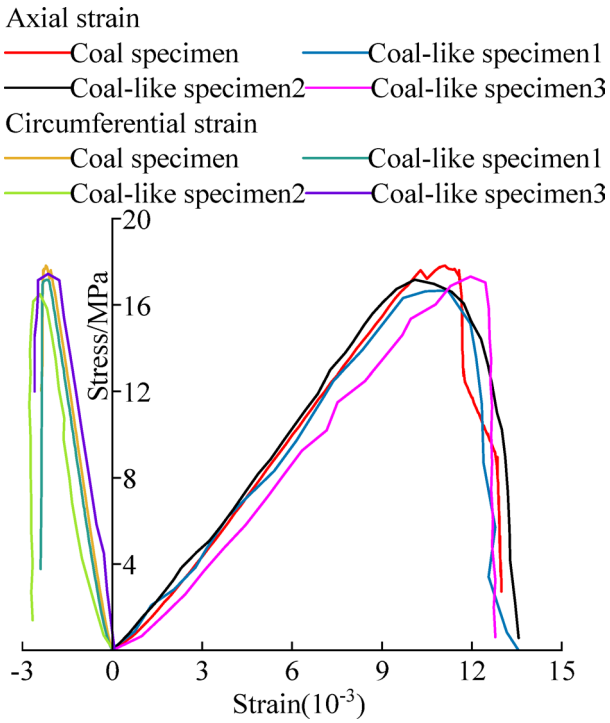

Fig. 1. Curves of measured mechanical parameters of coal-like specimen and coal specimen.

during the cyclic L-U process. The number of disturbances encountered by the coal is analogized as the number of L-U cycles, while dynamic disturbances such as fault slips and roof collapses are abstracted as impact dynamic loading.

The study first conducts quasi-static uniaxial cyclic L-U tests, using the maximum loading stress and the number of L-U cycles as variables, to prepare coal-like specimens with varying degrees of damage. Subsequently, impact dynamic loading is applied to the damaged specimens until failure occurs. The full-process deformation evolution and final impact-induced fracturing characteristics of the specimens are then analyzed. According to relevant research findings[23], during the loading process of coal, the stress-strain curve transitions from the compaction stage to the elastic stage when the applied load reaches approximately 30% of its UCS. When the load reaches about 70% of the UCS, the curve enters the yield stage from the elastic stage. Based on this, the maximum loading stresses in this test were set to 0.7, 0.5, and 0.3 times the UCS, corresponding to 2500 kN, 1750 kN, and 1000 kN, respectively. Taking into account the actual mining layout and the potential number of disturbances experienced by the coal mass, the number of cyclic L-U cycles was set to 5, 4, and 3, respectively. It is generally accepted that when the specimen strain rate is less than 10^{-5}/s, the loading condition is considered static, whereas a strain rate greater than 10^{-3}/s corresponds to dynamic loading[24]. Accordingly, the loading rate

during the quasi-static cyclic L-U process was set to 0.00125 mm/s, resulting in a specimen strain rate of 2.77×10^{-6}/s, which meets the criteria for static loading. For the dynamic axial compression tests under impact loading, the loading rate was set to 0.9 mm/s, corresponding to a specimen strain rate of 2×10^{-3}/s, thereby satisfying the dynamic loading condition. The test scheme is illustrated in Fig. 2.

3D laser scanning scheme

Principle of 3D laser scanning

3D laser scanning technology is a high-precision, non-contact measurement method based on active laser ranging principles. By combining high-speed rotational scanning with angular calculations, it enables rapid acquisition of large-scale, high-density 3D spatial data of the target surface within a short period of time. This technology enables the simultaneous acquisition of a large number of spatial coordinates, reflection intensities, and texture features of the target surface. The scanning results are presented in the form of point cloud data, providing a reliable data foundation for the subsequent construction of high-resolution 3D visualization models[25–27]. The core principle of 3D laser scanning technology lies in the use of a laser scanner that takes its internal laser emission point as the origin of the measurement coordinate system. By measuring the time-of-flight or phase shift of the laser beam between emission and return, the propagation distance of the laser beam is calculated. Combined with real-time recording of the horizontal and vertical scanning angles, the spatial coordinates of each measured point can be reconstructed through the conversion between polar and Cartesian coordinate systems. Typically, a 3D laser scanner establishes a right-handed Cartesian coordinate system with the laser emission point as the origin. The z-axis is defined as positive in the vertically upward direction and lies within the vertical scanning plane. The x-axis and y-axis together form the horizontal plane, with the positive y-axis pointing toward the measured object, as illustrated in Fig. 3. By utilizing the measured distance along with the horizontal and vertical angles, the 3D coordinates of each point on the target object can be inversely calculated using Eq. (1). This method offers significant advantages in capturing surface deformation characteristics of structures and is particularly well-suited for high-precision recording and analysis of coal or surrounding rock deformation processes in the complex environments of underground mines.

$$\begin{aligned} S &= 1/2c\Delta t \\ x &= S\cos\theta\sin\alpha \\ y &= S\cos\theta\cos\alpha \\ z &= S\sin\theta \end{aligned} \tag{1}$$

where, S is the distance between the laser emission point and each point on the measured object; c is the speed of light; t is the time interval from laser emission to return; θ is the vertical angle; φ is the horizontal angle.

Leica RTC360 3D laser scanner

In this study, the Leica RTC360 3D laser scanner was employed to monitor the deformation of the coal-like specimens. The device is equipped with a three-camera system, each lens having a resolution of 12 megapixels,

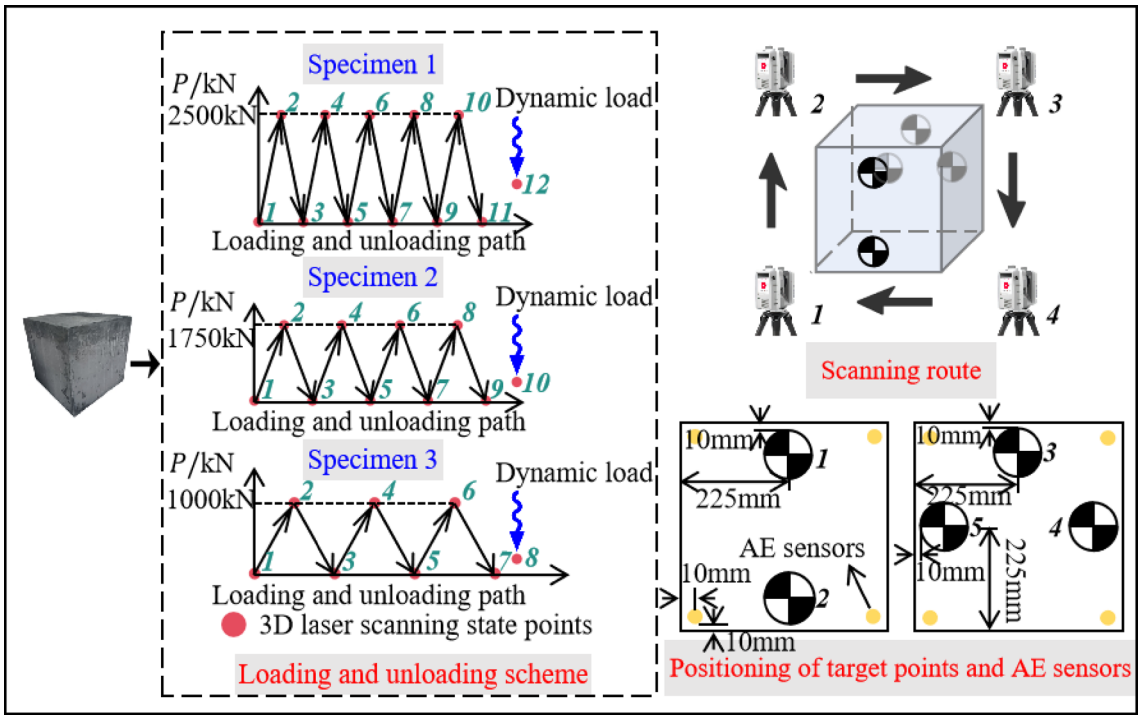

Fig. 2. Test scheme.

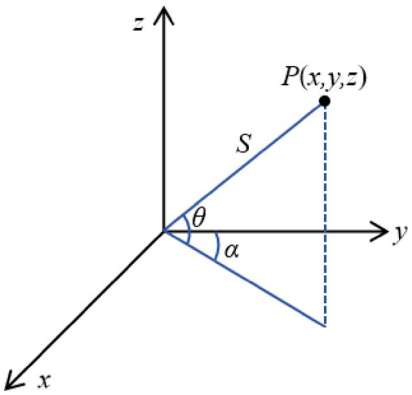

Fig. 3. Spatial coordinate system of the 3D laser scanning system.

Fig. 4. Leica RTC360 3D laser scanner.

System parameter	Value	System parameter	Value
Scanning range	0.5 ~ 130 m	Laser wavelength	1550 nm
Scanning rate	2 million points/s	Maximum pulse energy	1.5 μJ
Resolution	3 mm@10m	Pulse duration	0.5 ns
Ranging accuracy	1 mm + 10ppm	Maximum pulse repetition frequency	2 MHz
Angular accuracy	18”	Noise range	0.4 mm@10m
Positional accuracy	1.9 mm@10m	Operating temperature	− 5 ~ 40° C

Table 3. Technical parameters of Leica RTC360 3D laser scanner[28–30].

resulting in a total of 36 megapixels. It is capable of generating panoramic images with up to 432 million pixels and offers a panoramic field of view of 360° horizontally and 300° vertically. The scanner is equipped with TruRTC real-time reality capture technology, VIS visual inertial tracking, and SmartReg intelligent registration technology, enabling rapid and high-precision point cloud stitching and automatic registration within a short period. These features significantly enhance data acquisition efficiency and operational convenience. The scanner device is shown in Fig. 4, and its key technical parameters are listed in Table 3.

3D laser scanning technical scheme

The implementation process of the 3D laser scanning technology primarily consists of four stages: preliminary preparation, field scanning, data processing, and results application. The overall technical route is illustrated in Fig. 5.

Prior to initiating the scanning operation, it is essential to plan the scanning path and determine the placement of the scanner based on the specimen’s geometric characteristics and the target scanning area. This ensures comprehensive 360° panoramic data coverage while minimizing the acquisition of redundant data. Given that laser scanning data registration typically requires the formation of a closed loop, four scanning stations were arranged along the diagonal of the specimen to form a circular scanning path. The specific layout is illustrated in Fig. 2. After completing the scan at each station, the scanner is sequentially moved to the next predetermined position along the planned route, and the scanning process is repeated until full coverage of the target area is achieved. To improve the quality of point cloud registration, it is necessary to reasonably place target points on the specimen surface to enhance data recognition and alignment accuracy. In this test, target points were

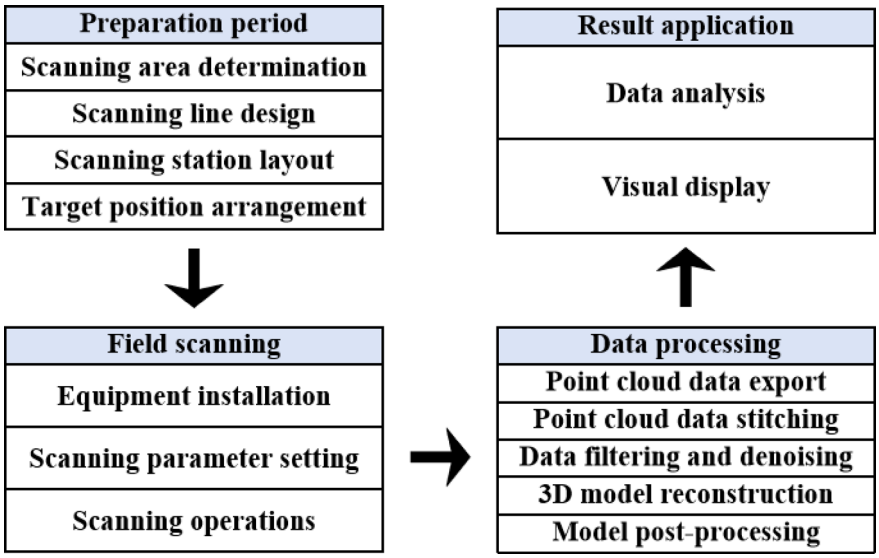

Fig. 5. Flow chart diagram.

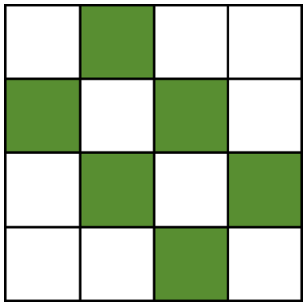

Fig. 6. Registration quality matrix.

arranged on both lateral surfaces of the specimen, with their specific locations shown in Fig. 2. Meanwhile, a total of eight acoustic emission (AE) sensors were arranged at the corner positions located 10 mm away from the specimen edges, enabling synchronous monitoring of AE signals throughout the testing process. The layout of the AE sensors is also illustrated in Fig. 2.

The scanning operation consists of multiple stages. First, an initial scan is conducted prior to the quasi-static cyclic loading, serving as a reference baseline for the specimen's initial condition. Subsequently, a scan is performed after each L-U cycle to record the deformation state of the specimen at each stage. Finally, a post-impact scan is conducted after the application of the dynamic load that causes specimen failure, in order to capture data on the failure morphology. Accordingly, a total of 12, 10, and 8 scans were performed for specimens 1, 2, and 3, respectively. After the scanning is completed, the scanner should return to the initial measurement point to verify the completeness and alignment integrity of the acquired data. The scanning process is considered finished once the data stitching is confirmed to be complete and the dataset is verified to be intact. During the test, high-precision total station technology was simultaneously employed for deformation monitoring, serving as a comparative reference to validate the results obtained from the 3D laser scanning.

The quality of data processing directly affects the subsequent 3D model construction and analysis results. Point cloud data collected by the laser scanner were exported and stored on a computer. Cyclone Register 360 software was used to perform high-precision, fully automated intelligent registration of point clouds from multiple scan positions. During this process, to ensure data accuracy, statistical outlier removal filtering was first applied to eliminate noise points and abnormal measurements. Then, the Iterative Closest Point (ICP) algorithm was used to achieve precise alignment of sequential scans, ensuring consistency of deformation data across different loading stages. Figure 6 presents the point cloud registration quality matrix for this test, with all error metrics meeting the relevant requirements. After registration, surface reconstruction algorithms were utilized to generate continuous 3D models. Post-processing operations, including mesh smoothing, topology repair, and texture mapping, were then performed to improve visualization quality and geometric consistency. This procedure ultimately provided reliable 3D deformation fields for quantitative analysis of specimen deformation and failure characteristics.

Finally, dimensional measurements were performed on the 3D models generated from the point cloud data. By comparing the spatial coordinate changes of key measurement points across different scanning stages, fully automated deformation calculation and visualization analysis of the specimens under various loading and unloading conditions were achieved. By comparing with the initial state model, the deformation evolution and failure distribution characteristics throughout the entire loading-unloading-impact process of the specimens can be systematically revealed.

Analysis of deformation evolution

To comprehensively reveal the deformation response mechanisms and structural degradation characteristics of coal throughout the entire testing process, this section employs high-precision 3D laser scanning technology combined with total station measurements for dynamic monitoring and analysis of the specimens' full deformation process. To explore the differences in coal structure responses and failure evolution paths under varying loading conditions.

Evolution law of stress–strain curve

The axial full stress–strain curves of each specimen are shown in Fig. 7. It can be observed that, at the early stage of the first loading under relatively low stress levels, all three groups of specimens exhibited significant plastic deformation in the loading direction, showing pronounced nonlinear characteristics. This behavior was attributed to the presence of numerous pre-existing microcracks, which caused the specimens to rapidly enter the compaction stage under load, with crack closure leading to plastic deformation. As the tests progressed, the second loading curve became steeper than the first, while the internal cracks of the specimens continuously experienced compaction and propagation. Consequently, the loading and unloading paths of each cycle could not coincide, and the stress-strain relationship was no longer one-to-one. With increasing cycle numbers, the curves gradually shifted toward larger strains, forming successive plastic hysteresis loops. In the later stages of cyclic progress, the cumulative deformation of the specimens increased, the hysteresis loops became denser, and the irreversible deformation grew progressively with the number of cycles. After the application of dynamic impact loading, all three groups of specimens rapidly reached the stress peak, and the post-peak curve initially dropped almost vertically, indicating that all specimens experienced impact-induced failure.

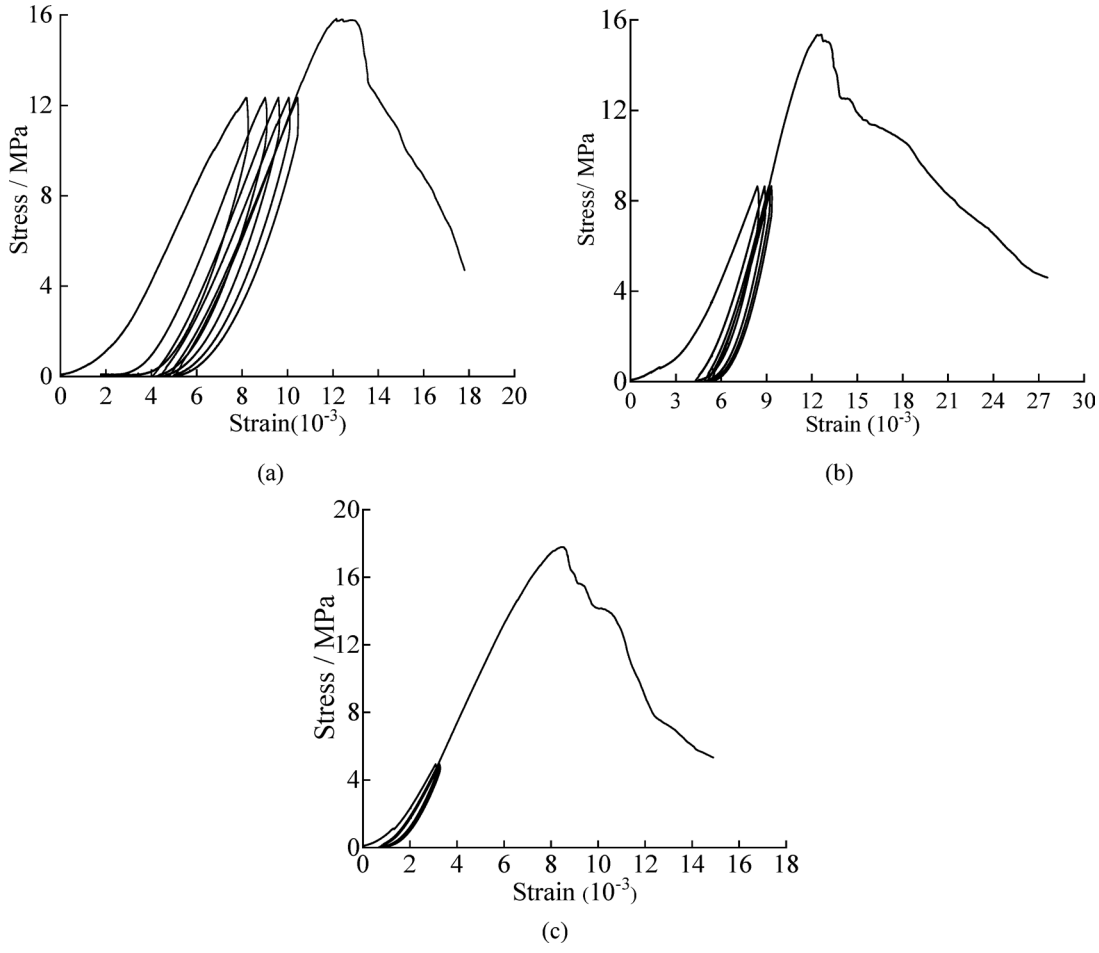

Fig. 7. Stress-strain curves (**a**) Specimen 1 (**b**) Specimen 2 (**c**) Specimen 3.

Deformation evolution analysis based on 3D laser scanning monitoring

To systematically reveal the deformation evolution of specimens under quasi-static cyclic L-U and subsequent dynamic impact loading, the deformation data at each stage were extracted and calculated based on the 3D laser scanning point clouds. Specifically, the subfigures in Figs. 8 and 9, and 10 were obtained as follows: (a) represents the cumulative overall deformation throughout the entire testing process, calculated from the displacement variations of each stage; (b) shows the net deformation produced during each complete L-U cycle, determined from the displacement difference between the start and end of each cycle; (c) presents the deformation produced during each loading stage, obtained from the displacement variation between the beginning of the cycle and the peak load point; and (d) illustrates the elastic recovery during each unloading stage, derived from the displacement rebound between the peak load point and the end of unloading.

As shown in Fig. 8a, during the cyclic loading process up to the yield stage, specimen 1 exhibits a continuous accumulation of overall deformation with increasing cycle numbers, demonstrating a clear characteristic of progressive damage accumulation. Eventually, under the application of impact dynamic loading, the specimen experienced severe impact-induced failure, with a maximum deformation of 40.3247 mm, significantly greater than that observed during the preceding quasi-static cyclic L-U stage. Further analysis of Fig. 8b reveals that, prior to the application of impact dynamic loading, the deformation induced by each complete L-U cycle increased progressively with the number of cycles, and the rate of increase also exhibited a growing trend. Specifically, the deformation induced during the fifth L-U cycle reached 2.9 times that of the first cycle, indicating that repeated loading and unloading disturbances led to the continuous initiation, propagation, and coalescence of microcracks within the specimen. As a result, structural stiffness gradually declined, and the degree of damage progressively increased.

During each individual L-U cycle, the specimen exhibits a certain degree of deformation upon completion of the loading phase. After unloading, a partial recovery of elastic deformation occurs. As shown in Figs. 8c and d, with the increase in the number of L-U cycles, the residual deformation induced by each individual loading process continues to increase, and the rate of growth gradually accelerates. This is primarily attributed to the continuous propagation and coalescence of internal microcracks during the cyclic L-U process after the specimen enters the yield stage, leading to cumulative damage and a progressive reduction in structural stiffness. During

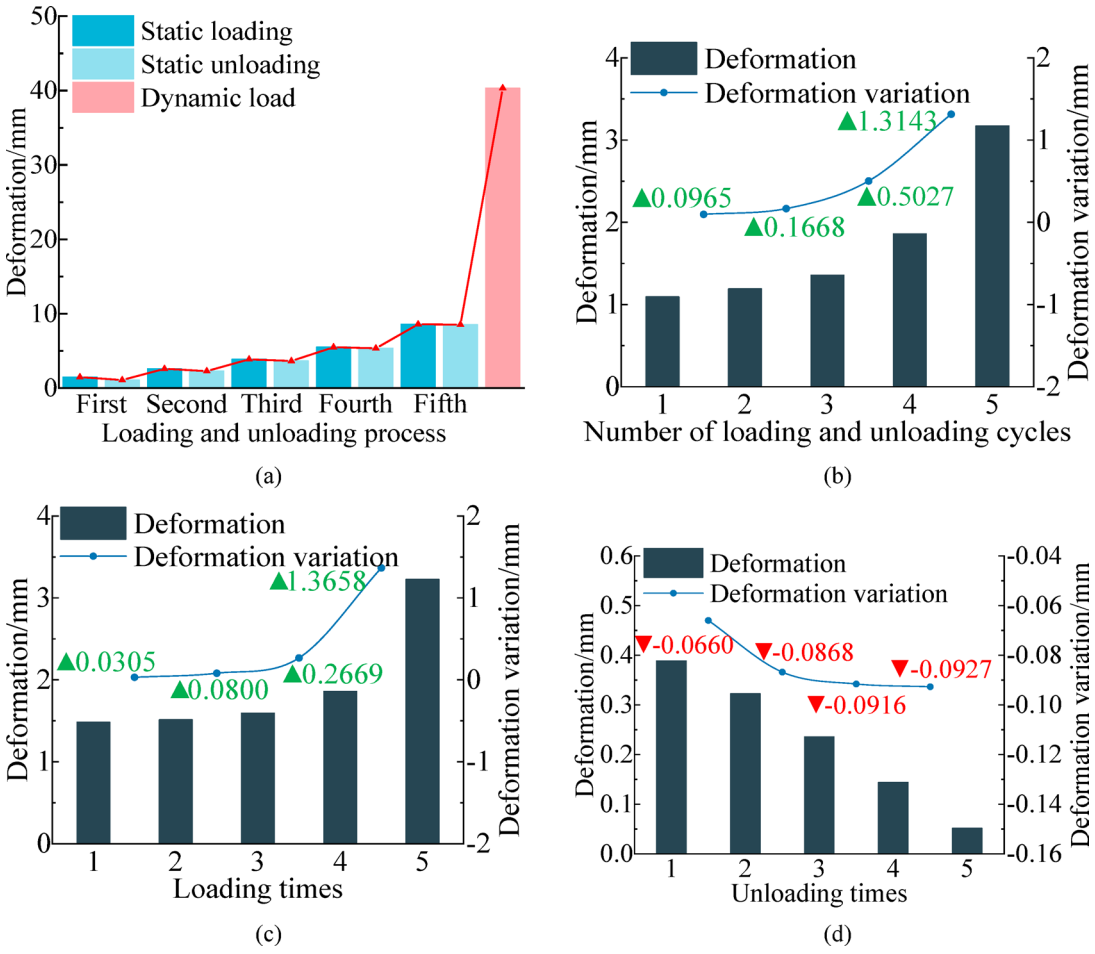

Fig. 8. Deformation of specimen 1 (**a**) The overall deformation during the test process (**b**) The deformation during each complete cycle (**c**) The deformation produced by loading during each cycle (**d**) The elastic deformation recovery produced by unloading during each cycle.

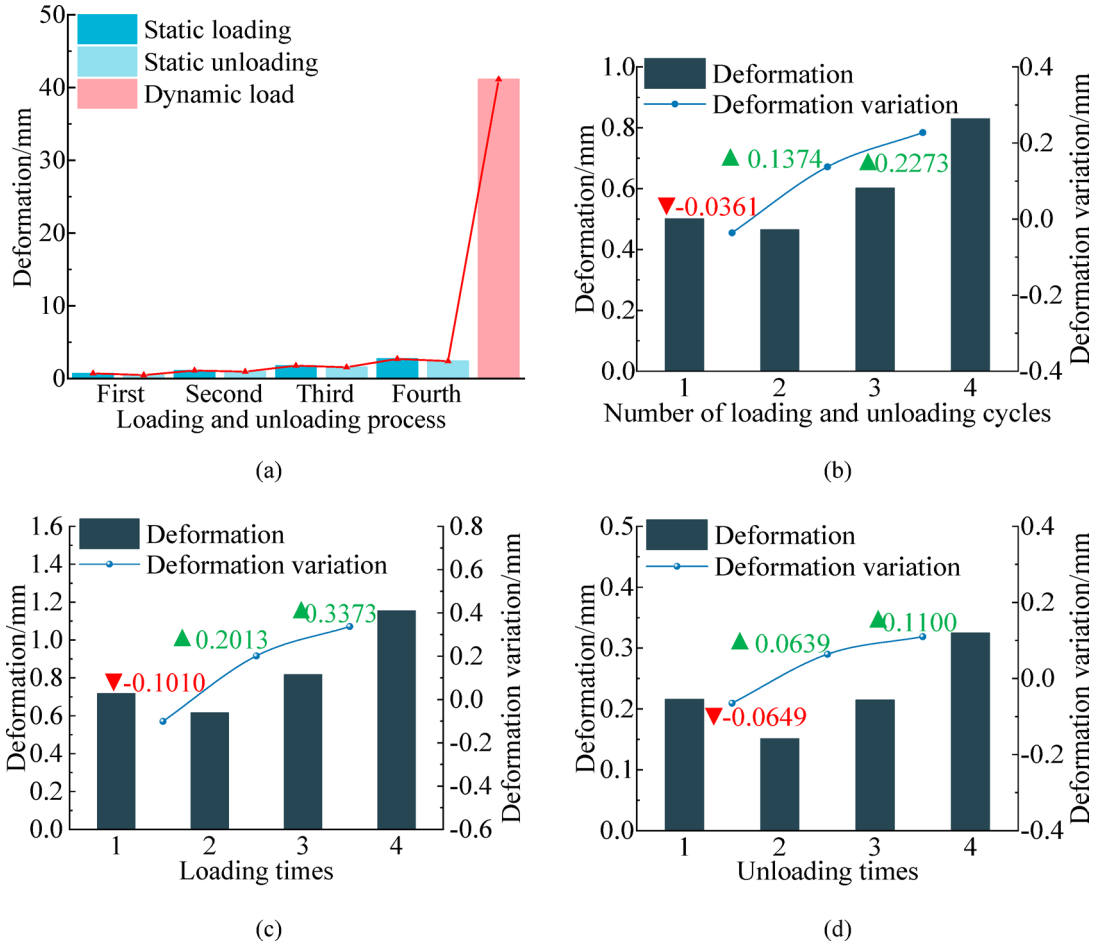

Fig. 9. Deformation of specimen 2 (**a**) The overall deformation during the test process (**b**) The deformation during each complete cycle (**c**) The deformation produced by loading during each cycle (**d**) The elastic deformation recovery produced by unloading during each cycle.

the unloading stage, the expansion and accumulation of internal cracks within the specimen significantly weaken its elastic recovery capacity. As a result, the amount of elastic deformation recovered after each unloading cycle gradually decreases, and the rate of decrease progressively accelerates. The above phenomena indicate that the coal has entered a highly nonlinear deformation region during the yield stage, exhibiting failure characteristics dominated by plastic deformation.

During the cyclic L-U process, the maximum loading stress of specimen 2 was controlled within the elastic stage. The overall deformation under each L-U condition is shown in Fig. 9a. With the increase in the number of cycles, the deformation of specimen 2 continued to grow; however, the overall magnitude was smaller than that of specimen 1, which was loaded to the yield stage. Under the final impact dynamic loading, specimen 2 also experienced impact-induced failure, with a maximum deformation of 41.1156 mm, slightly higher than that of sspecimen 1. This indicates that specimen 2 exhibited a greater energy storage capacity in the earlier stage, leading to a more intense failure upon impact. As shown in Fig. 9b, prior to the application of impact dynamic loading, the deformation during each complete L-U cycle of specimen 2 initially decreased slightly and then gradually increased with the number of cycles. The overall variation ranged from 7.2% to 37.8%. This is because, under cyclic loading within the elastic stage, the specimen undergoes continuous compaction of pre-existing microcracks and the initiation and propagation of new cracks. Under this complex interaction, the internal damage of the specimen initially decreases due to crack closure, but subsequently increases as loading continues, leading to a gradual increase in overall deformation.

Figure 9c and d further illustrate the evolution patterns of the loading-induced deformation and the elastic recovery during unloading in each individual L-U cycle of specimen 2. It is evident that both parameters exhibit a trend of initially decreasing and subsequently increasing with the number of cycles. During the second L-U cycle, the deformation generated during the loading phase was less than the corresponding elastic recovery during unloading. However, starting from the third cycle, the deformation induced by loading exceeded the elastic recovery in the unloading phase. As a result, the overall deformation of the specimen exhibited a trend of initially decreasing and then increasing. The above phenomena indicate that the specimen loaded within the elastic stage undergoes a complex process involving the compaction of pre-existing microcracks and the initiation and propagation of new cracks. In the early stages, the compaction of original cracks dominates,

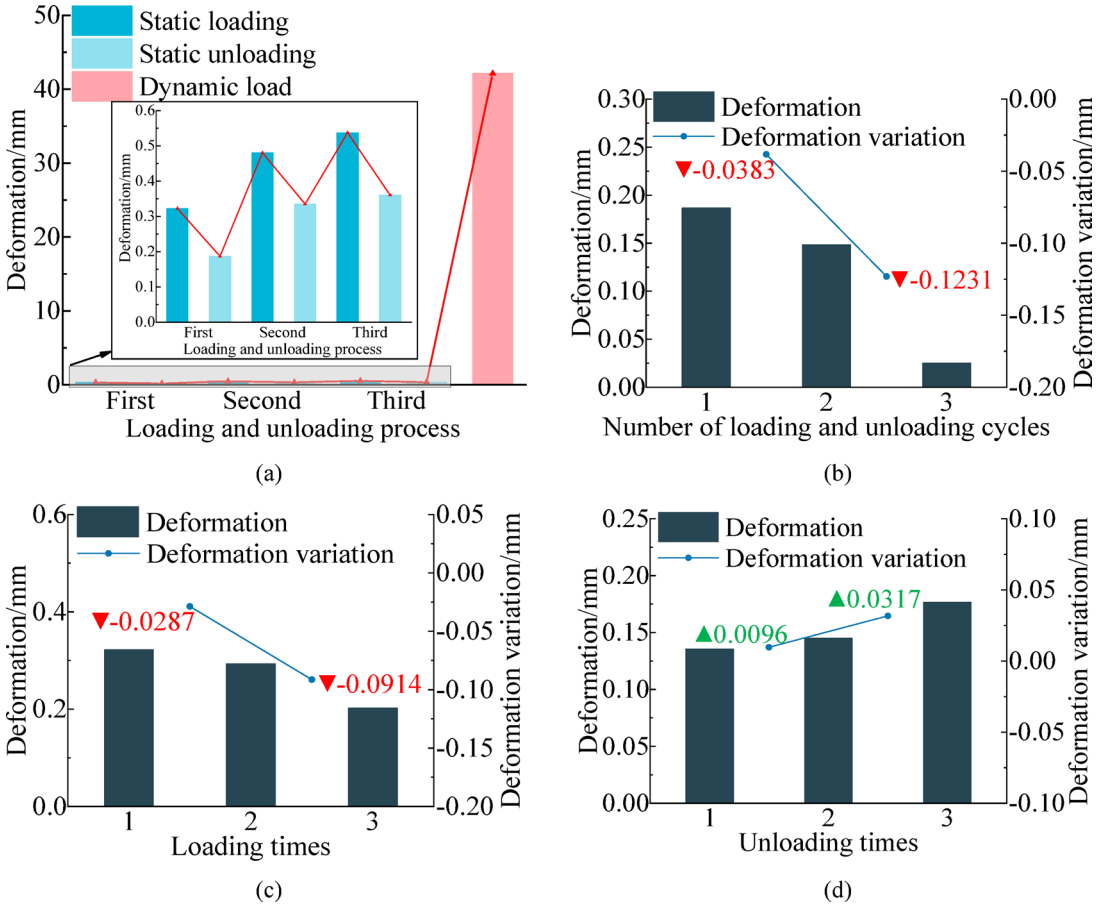

Fig. 10. Deformation of specimen 3 (**a**) The overall deformation during the test process (**b**) The deformation during each complete cycle (**c**) The deformation produced by loading during each cycle (**d**) The elastic deformation recovery produced by unloading during each cycle.

leading to a reduction in overall damage and a decrease in deformation. However, as the number of L-U cycles increases, newly formed cracks gradually initiate and propagate, eventually surpassing the compaction effect of the original cracks. Consequently, the total deformation begins to increase again. It can thus be concluded that the compaction and propagation of fracture structures alternately dominated the damage evolution of specimen 2 during the cyclic loading process. This reflects a dynamic transition in the governing mechanism-from initial crack compaction to progressive crack propagation.

During the cyclic L-U process, specimen 3 remained in the compaction stage throughout. As shown in Fig. 10a, its overall deformation was significantly lower than that of specimens 1 and 2. Under the final impact dynamic loading, specimen 3 also experienced severe failure, with a maximum deformation of 42.1180 mm. This indicates that, although the specimen exhibited relatively small deformation in the earlier stages, it still demonstrated a high-energy release characteristic during the impact phase. As shown in Fig. 10b, prior to the application of dynamic impact loading, the deformation during each complete L-U cycle of specimen 3 exhibited a monotonically decreasing trend, with the rate of reduction progressively increasing. This indicates that the internal fractures within the specimen were primarily dominated by compaction and closure, leading to a gradual reduction in damage extent and an enhanced tendency toward structural stabilization.

Figure 10c and d further illustrate that, with the increase in the number of cycles, the deformation experienced by specimen 3 during the loading phase gradually decreased, while the elastic recovery during the unloading phase progressively increased. Moreover, the magnitude of elastic recovery showed an expanding growth trend. This phenomenon suggests that specimen 3 experienced a structural reinforcement effect during cyclic loading. The gradual compaction of original microcracks enhanced the material stiffness and reduced the rate of damage evolution, which explains its different behavior compared with the other specimens.

Deformation evolution analysis based on total station monitoring points

To validate the reliability of the 3D laser scanning results, high-precision displacement monitoring of key target points on the specimens was simultaneously conducted using total station technology throughout the test. Two monitoring points were selected in total, namely target point 1 and target point 2, which are located along the axial centerline of the specimen as shown in Fig. 2. Since the specimen is subjected to axial loading, its axial deformation becomes increasingly pronounced as the test progresses. This is reflected in the significant changes

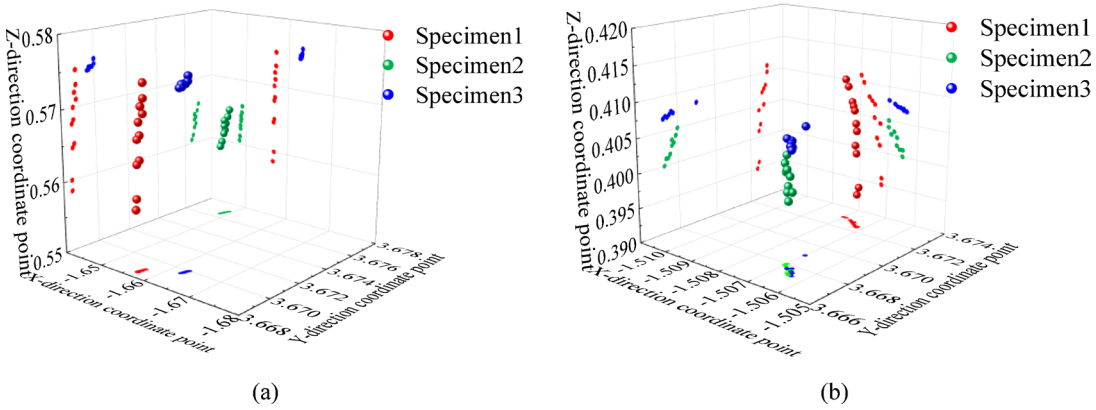

Fig. 11. Spatial coordinates of each monitoring point (**a**) Point 1 (**b**) Point 2.

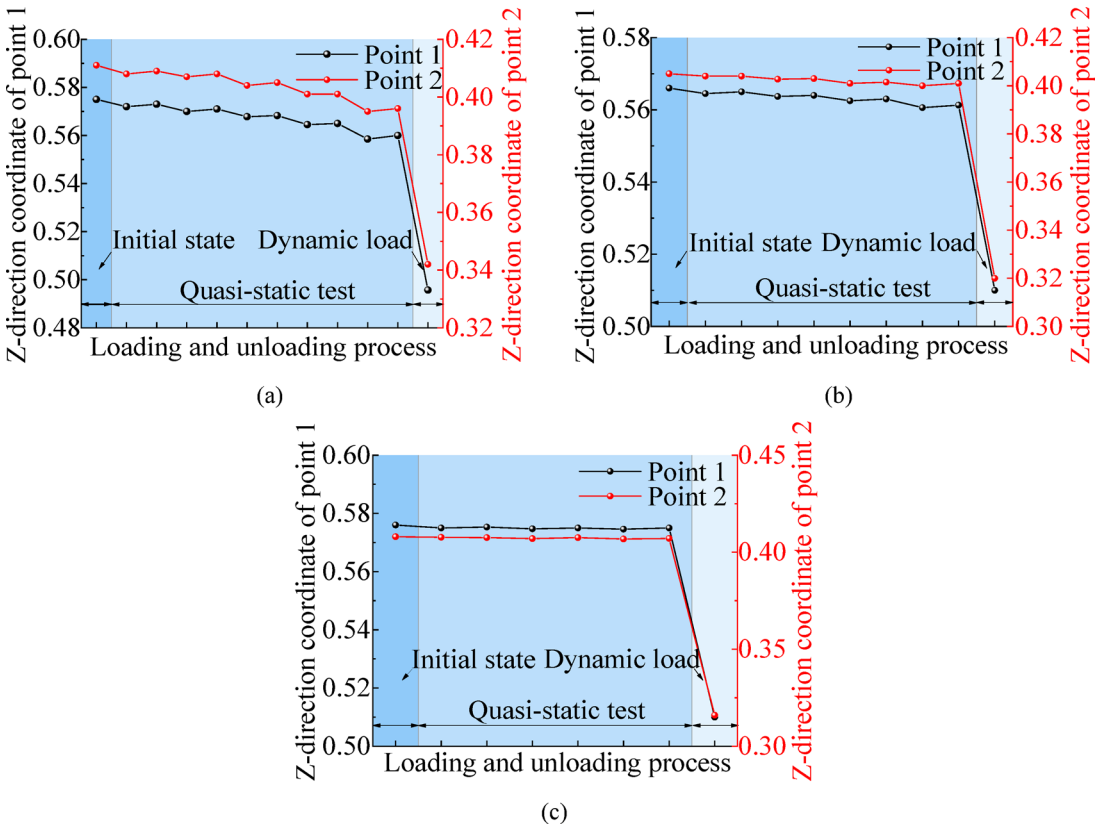

Fig. 12. Spatial coordinate positions monitored by total station (**a**) Specimen 1 (**b**) Specimen 2 (**c**) Specimen 3.

observed in the Z-axis direction of the 3D spatial coordinates at each monitoring point, as illustrated in Fig. 11. During the cyclic L-U process, the Z-axis coordinate values of the specimen gradually decrease during the loading stages, indicating significant axial compression under external loads. In the subsequent unloading stages, due to partial recovery of elastic deformation, the Z-axis coordinates exhibit a certain degree of rebound. Overall, the variation trends of Z-axis displacement during loading and unloading effectively reflect the elastoplastic mechanical response characteristics of the material.

Figure 12 compares the axial displacement variations among the three specimens. As shown in the figure, during the quasi-static cyclic process, specimen 1 exhibits the most significant displacement fluctuations, indicating the most severe structural damage. Specimen 2 shows relatively stable variations, while specimen 3 displays the smallest displacement amplitude, suggesting it experienced the least disturbance. After the application of impact dynamic loading, all three specimens experienced sudden and substantial failure, evidenced by a sharp drop in the Z-axis coordinates of the target points. This confirms the devastating effect of impact loading on structural integrity. To further validate the accuracy of the 3D laser scanning results, a

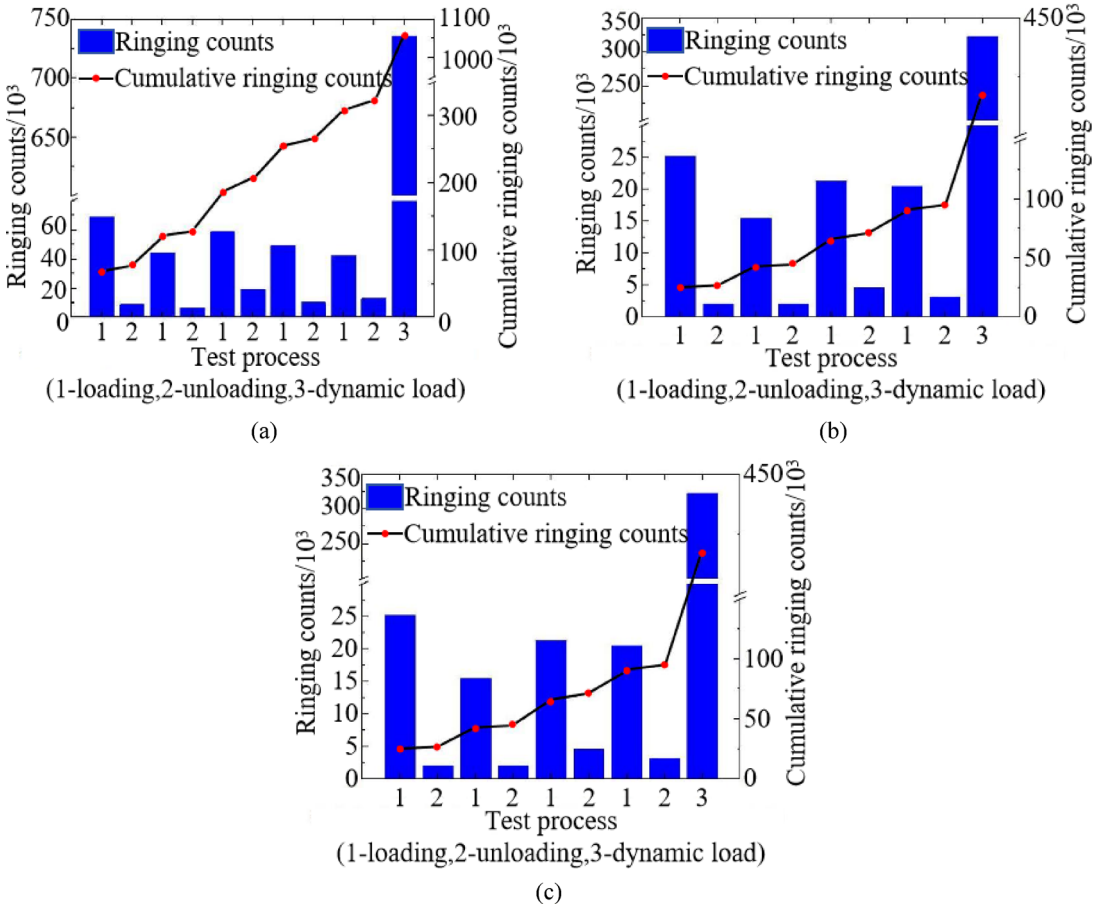

Fig. 13. AE ringing counts (**a**) Specimen 1 (**b**) Specimen 2 (**c**) Specimen 3.

No.	First cycle		Second cycle		Third cycle		Forth cycle		Fifth cycle		Dynamic load
	Loading	Unloading	Loading	Unloading	Loading	Unloading	Loading	Unloading	Loading	Unloading	
Specimen1	14,832	6712	17,983	7039	19,968	7298	21,808	7390	25,790	7821	305,236
Specimen2	8179	2064	9498	2298	9867	2587	10,638	2845	–	–	160,939
Specimen3	5587	1578	5945	1632	6034	1745	–	–	–	–	91,647

Table 4. AE ringing counts.

quantitative comparison was conducted with the total station measurements at the same monitoring points. The axial displacement curves obtained from both techniques showed a high degree of consistency, with the maximum deviation less than 2.5%. The total station monitoring data closely align with the overall trends and deformation patterns observed from the 3D laser scanning results, further validating the accuracy and reliability of 3D laser scanning technology for deformation measurement.

Damage evolution analysis

To further investigate the damage evolution characteristics of the specimens during the testing process, AE monitoring was conducted simultaneously to assess internal damage development. The statistical results of AE ringing counts are presented in Fig. 13; Table 4. The results indicate that during the quasi-static L-U cycles, the AE ringing counts recorded during the loading phases were significantly higher than those during the unloading phases for all three specimens. In contrast, during the dynamic impact loading stage, the ringing counts far exceeded the total accumulated during the entire quasi-static L-U process, suggesting that the impact load induced a more intense process of crack propagation and energy release.

A comparative analysis of the three specimens shows that the cumulative ringing counts of specimen 1 during the cyclic L-U stage is 2.8 times that of specimen 2 and 5.98 times that of specimen 3. This indicates that with increasing cycle numbers and loading stress levels, the degree of damage in the specimens intensifies significantly, accompanied by increasingly frequent AE activity. During the L-U stage, specimen 1 exhibits a distinct stepwise surge in ringing counts, indicating that it is in an unstable fracture development phase.

Internal cracks continuously propagate and coalesce, ultimately leading to the formation of macroscopic fractures. Although the ringing counts of specimen 2 increases during the cyclic loading process, it remains at a relatively low level overall, indicating that the specimen is in a stable microcrack propagation stage, where crack development is mainly characterized by initiation and localized growth. Specimen 3 exhibits the lowest ringing counts and the slowest growth trend, indicating that it predominantly remains in a compaction state during the cyclic loading process. The original internal fractures gradually close, and the structural integrity tends toward stabilization.

Furthermore, the AE monitoring results exhibit a clear correspondence with the deformation characteristics captured by 3D laser scanning. During the compaction stage, both the low AE activity and limited deformation indicate the closure of initial microcracks. As the specimens entered the elastic and yield stages, AE ringing counts increased significantly, matching the progressive accumulation of deformation observed in the 3D deformation fields. At the failure stage under dynamic impact loading, the sharp surge in AE activity coincided with the rapid formation of macroscopic fractures identified in the post-impact 3D scanning results. This consistency demonstrates that AE parameters provide dynamic internal damage information, while 3D laser scanning captures the external deformation process, and their combined application offers a more comprehensive understanding of the coal-like specimens' damage and failure mechanisms.

Given that the damage evolution of coal and rock masses is closely related to the development of internal cracks, the AE ringing counts can serve as an important indirect indicator of damage severity. To quantitatively assess the contribution of the cyclic loading stage to the overall damage of the specimen, the concept of "damage contribution ratio" is introduced, defined as the ratio of the total AE ringing counts during the cyclic loading stage to the total AE ringing counts recorded throughout the entire test. The calculation formula is as follows:

$$D = \frac{N_1}{N_1 + N_2} \tag{2}$$

where, D is the damage contribution ratio; N_1 is the total AE ringing counts during the cyclic L-U stage; N_2 is the total ringing counts during the dynamic loading stage.

According to Eq. (2), the damage contribution ratios during the cyclic L-U stage for the three specimens were calculated to be 19.8%, 22.8%, and 25.7%, respectively. These results indicate that the stress levels and the number of loading cycles experienced during the quasi-static loading phase have a significant influence on the damage accumulation process of the specimens. With increasing peak loading levels and a greater number of loading cycles, internal cracks in the specimens progressively propagate, leading to deeper damage and a significantly greater contribution of the cyclic loading stage to the final structural failure. This trend demonstrates that under repeated cyclic disturbances, the structural integrity of coal-like materials continuously deteriorates, laying the groundwork for severe failure triggered by subsequent impact loading. It further confirms the critical role of loading history in the damage evolution and energy release behavior of coal and rock masses. The quantified results of the damage contribution ratio provide valuable support for understanding the mechanical response mechanisms of coal under repeated mining-induced disturbances and for improving disaster prediction.

Macroscopic failure characteristics

To thoroughly reveal the failure modes and their evolution patterns of coal specimens under cyclic disturbance and impact loading, high-precision deformation cloud maps of the three specimens before and after impact failure were obtained using 3D laser scanning technology, as shown in Fig. 14. Through comparative analysis, it can be observed that specimens subjected to relatively low loads during the preliminary quasi-static cyclic L-U stage exhibit smaller cumulative deformations and lower degrees of structural damage, indicating that they maintain a higher level of structural integrity under low load conditions. However, under the subsequent impact dynamic loading, these specimens exhibit more severe impact responses, with a significant increase in overall deformation, higher concentration of localized deformation, and markedly intensified damage. Based on the 3D point cloud data, the deformation magnitudes in the maximum deformation zones of the three specimens were further extracted and calculated as 40.325 mm, 41.116 mm, and 42.118 mm, respectively, indicating a trend that specimens with lower initial damage levels exhibited greater final deformation during impact failure. This result indicates that although the specimens subjected to lower loading levels experienced less initial damage under repeated disturbance loads, they may have accumulated more elastic energy during the cyclic loading process, which subsequently led to a more intense failure response upon the application of impact loading.

After the application of impact dynamic loading, all three specimens exhibited typical macroscopic failure characteristics dominated by impact-induced splitting, with their failure modes showing strong consistency, as illustrated in Fig. 15.

At the moment of impact dynamic loading application, the dynamic stress wave first propagates to the top of the specimen, generating a loud audible sound while rapidly initiating a visible primary crack in the upper region. Subsequently, the primary crack propagates downward at a certain angle, inducing secondary splitting cracks at the crack tip. Ultimately, multiple through-going cracks develop from top to bottom, exhibiting a typical axial splitting failure pattern. Throughout the entire process, the fractures predominantly align along the loading direction, with vertical cracks spaced at intervals, reflecting the brittle response behavior of the coal structure under impact loading. A further lateral comparison of the failure differences among the three specimens reveals that the initial damage degree has a significant impact on the final failure morphology. Specimens with lower damage levels during the early quasi-static cyclic phase exhibit higher impact failure intensity during the impact stage, characterized by more complex and dense fracture networks and more thorough integrity loss. This indicates that low-damage specimens possess a stronger energy storage capacity during the early stages,

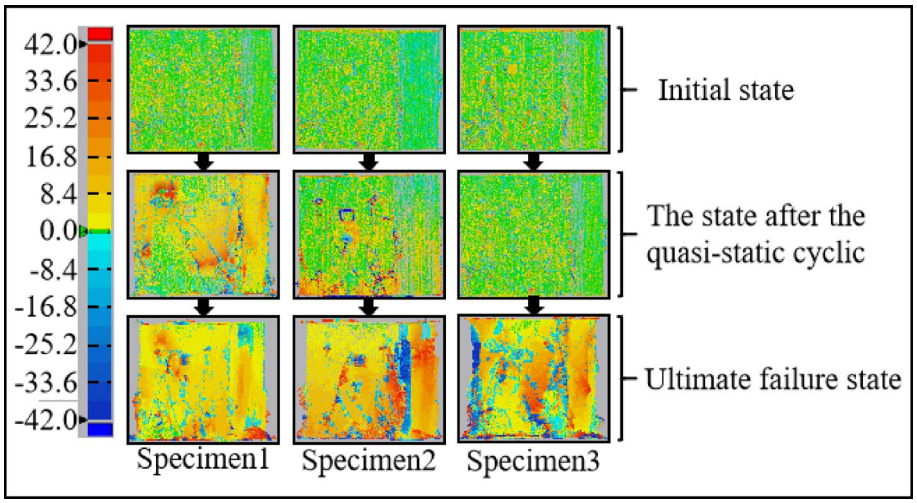

Fig. 14. Deformation cloud maps before and after impact failure.

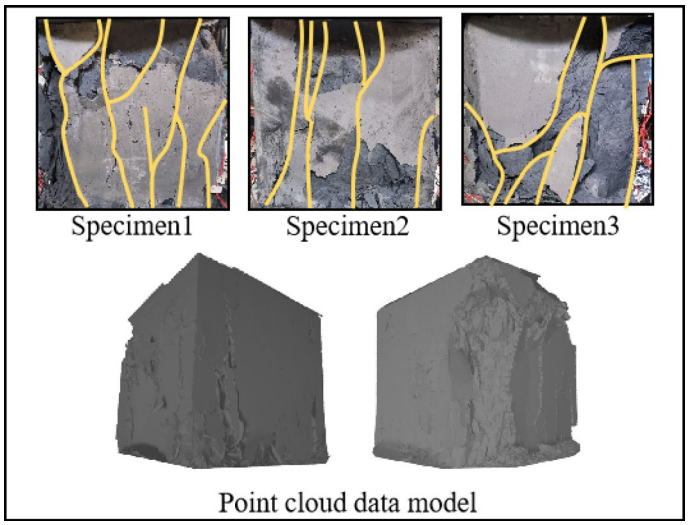

Fig. 15. Macroscopic impact fracture characteristics.

resulting in the release of greater destructive energy during the impact response, thereby producing more severe failure patterns.

In summary, the macroscopic failure characteristics of coal subjected to multiple cyclic disturbances and impact loads are influenced not only by the current loading conditions but also closely related to the prior structural damage state. Coal exposed to low-load disturbance environments in the early stages, despite exhibiting minimal initial damage, is more prone to severe failure under subsequent impact loading. This conclusion provides important theoretical insights and technical support for the prediction and prevention of rockburst hazards in coal mines.

Conclusions

Quasi-static uniaxial cyclic L-U tests under varying loading conditions and dynamic axial compression tests under impact loading were conducted on coal-like specimens. By integrating 3D laser scanning technology and total station deformation monitoring methods, the deformation evolution patterns and failure characteristics of the specimens throughout the entire testing process were analyzed. The main conclusions are summarized as follows:

(1) During the uniaxial cyclic L-U process, the loading intensity significantly influences the deformation response of the specimens. The maximum loading stress is the most critical factor affecting the deformation behavior of the damaged coal-like material. As the loading intensity progresses sequentially from the compaction stage, through the elastic stage, to the yield stage, the overall deformation of the specimen gradually increases, indicating that higher loading levels lead to greater structural degradation of the coal.

(2) With the increase in the number of cycles, the deformation of specimens loaded up to the yield stage continuously increases, with the rate of increase gradually accelerating. This indicates that in specimens entering the yield stage, damage cracks progressively extend and coalesce, accelerating structural deterioration. In contrast, specimens loaded to the elastic stage exhibit a decreasing trend in deformation during the initial cycles, followed by a gradual increase, reflecting an alternating dominance between the compaction of original microcracks and the initiation and propagation of new cracks. As the number of cycles increases further, the effect of new crack propagation becomes dominant, and the damage degree progressively intensifies. Meanwhile, specimens loaded to the compaction stage show a continuous decrease in deformation with an increasing rate of reduction, indicating that pre-existing cracks are further compacted during cyclic disturbance, resulting in reduced damage and enhanced structural stability.
(3) AE monitoring indicated that the coal-like material exhibited pronounced damage evolution characteristics during cyclic loading, with crack compaction and propagation alternately dominating the structural response. The damage contribution rate increased with both loading intensity and the number of cycles, significantly influencing the subsequent impact failure behavior.
(4) All three specimens exhibited typical splitting-type failure under impact dynamic loading, displaying consistent macroscopic failure modes. Notably, specimens with lower damage levels during the prior cyclic disturbance phase maintained higher structural integrity and thus possessed greater energy accumulation capacity. Upon triggering by the impact load, these specimens released larger amounts of energy, resulting in more intense impact failure, with more severe damage and more complex and dense fracture networks.
(5) This study employed the Leica RTC360 3D laser scanner to conduct high-precision monitoring of the entire deformation evolution process of coal-like specimens under quasi-static cyclic L-U and impact dynamic loading. The acquired point cloud data not only vividly and intuitively depicted the comprehensive 3D deformation characteristics of the specimen surface but also demonstrated high spatial resolution and field efficiency. The monitoring results showed good agreement with axial displacement trends measured by the total station, thereby validating the feasibility and reliability of this technology in rock mechanics testing.
(6) This study develops and validates a full-process 3D deformation monitoring method that integrates 3D laser scanning and total station technology. This innovation enables accurate, non-contact, and continuous tracking of specimen deformation and damage evolution throughout cyclic loading and dynamic impact testing. The findings not only deepen the understanding of coal deformation-failure mechanisms under multiple disturbances but also provide an advanced technical means with strong applicability for monitoring roadway stability, assessing impact risks, and guiding disaster prevention in coal mining engineering practice.
(7) Despite the valuable insights provided by this study, several limitations should be acknowledged. First, the prepared coal-like specimens, with dimensions of 450 mm×450 mm× 450 mm, inevitably introduce a scale effect compared to in-situ coal masses, which may influence stress distribution, crack evolution, and energy release characteristics. Second, although the coal-like material was proportioned to match the physical and mechanical properties of raw coal, differences in microstructure and mineral composition remain, potentially affecting the deformation and failure mechanisms. Third, the experimental boundary conditions, which include uniaxial cyclic L-U and simplified dynamic impact loading, cannot fully replicate the complex 3D stress environment encountered in underground mining. These limitations indicate that further validation through larger-scale model tests, in-situ monitoring, and numerical simulations is necessary. Nevertheless, the current results provide important references for understanding the fundamental mechanisms of coal damage evolution under multiple disturbances and hold significant implications for impact disaster prevention and control in coal mines.

Data availability

The data that support the findings of the study are available from the corresponding author upon reasonable request.

Received: 31 July 2025; Accepted: 11 December 2025
Published online: 06 January 2026

References

1. Betz, M. R., Partridge, M. D., Farren, M. & Lobao, L. Coal mining, economic development, and the natural resources curse. *Energy Econ.* **50**, 105–116 (2015).
2. Dai, S. & Finkelman, R. B. Coal as a promising source of critical elements: progress and future prospects. *Int. J. Coal Geol.* **186**, 155–164 (2018).
3. Cai, W. et al. A monitoring investigation into rock burst mechanism based on the coupled theory of static and dynamic stresses. *Rock Mech. Rock Eng.* **53**, 5451–5471 (2020).
4. Zhu, W. C., Li, Z. H., Zhu, L. & Tang, C. A. Numerical simulation on rockburst of underground opening triggered by dynamic disturbance. *Tunn. Undergr. Space Technol.* **25**(5), 587–599 (2010).
5. He, M., Cheng, T., Qiao, Y. & Li, H. A review of rockburst: Experiments, theories, and simulations. *J. Rock Mech. Geotech. Eng.* **15**(5), 1312–1353 (2023).
6. Xiao, P. et al. Mechanical properties and failure behavior of rock with different flaw inclinations under coupled static and dynamic loads. *J. Cent. South. Univ.* **27**(10), 2945–2958 (2020).
7. Zhou, Z., Li, X., Zou, Y., Jiang, Y. & Li, G. Dynamic Brazilian tests of granite under coupled static and dynamic loads. *Rock Mech. Rock Eng.* **47**, 495–505 (2014).
8. Zou, C., Wong, L. N. Y., Loo, J. J. & Gan, B. S. Different mechanical and cracking behaviors of single-flawed brittle gypsum specimens under dynamic and quasi-static loadings. *Eng. Geol.* **201**, 71–84 (2016).

9. Zhou, Z., Cai, X., Li, X., Cao, W. & Du, X. Dynamic response and energy evolution of sandstone under coupled static–dynamic compression: insights from experimental study into deep rock engineering applications. *Rock Mech. Rock Eng.* **53**, 1305–1331 (2020).
10. Wang, S. Y., Sloan, S. W., Liu, H. Y. & Tang, C. A. Numerical simulation of the rock fragmentation process induced by two drill Bits subjected to static and dynamic (impact) loading. *Rock Mech. Rock Eng.* **44**, 317–332 (2011).
11. Zhu, J. B., Liao, Z. Y. & Tang, C. A. Numerical SHPB tests of rocks under combined static and dynamic loading conditions with application to dynamic behavior of rocks under in situ stresses. *Rock Mech. Rock Eng.* **49**, 3935–3946 (2016).
12. Gong, F. Q. & Zhao, G. F. Dynamic indirect tensile strength of sandstone under different loading rates. *Rock Mech. Rock Eng.* **47**, 2271–2278 (2014).
13. Chen, Y., Zuo, J., Liu, D. & Wang, Z. Deformation failure characteristics of coal–rock combined body under uniaxial compression: experimental and numerical investigations. *Bull. Eng. Geol. Environ.* **78**, 3449–3464 (2019).
14. El-Omari, S. & Moselhi, O. Integrating 3D laser scanning and photogrammetry for progress measurement of construction work. *Autom. Constr.* **18**(1), 1–9 (2008).
15. Zhang, D. et al. Three-dimensional laser scanning for large-scale as-built surveying of 2022 Beijing winter olympic speed skating stadium: A case study. *J. Building Eng.* **59**, 105075 (2022).
16. Liu, J., Xu, D., Hyyppä, J. & Liang, Y. A survey of applications with combined BIM and 3D laser scanning in the life cycle of buildings. *IEEE J. Sel. Top. Appl. Earth Observations Remote Sens.* **14**, 5627–5637 (2021).
17. Ouyang, W. & Xu, B. Pavement cracking measurements using 3D laser-scan images. *Meas. Sci. Technol.* **24**(10), 105204 (2013).
18. Zhang, X. D., Hu, Y. Y., Zhang, X. Q. & Wu, Y. H. Study on the 3D information reconstruction and management of cultural relics based on the articulated arm scanner. *J. Digit. Inform. Manage.* **14**(1), 31–39 (2015).
19. Zhang, S., Wu, K., Wang, X. & Li, G. Discussion on application of 3D laser scanning technology to ground subsidence monitoring. *Coal Sci. Technol.* **11**(36), 92–95 (2008).
20. Kajzar, V., Kukutsch, R. & Heroldova, N. Verifying the possibilities of using a 3D laser scanner in the mining underground. *Acta Geodyn. Geomater.* **12**(1), 51–58 (2015).
21. Huang, X., Luan, Y. & Yan, Y. Monitoring deformation of headframe based on 3D terrestrial laser scanner. *Geotech. Invest. Surv*. **40**, 66–69 (2012).
22. Hu, Q. T., Zhang, S. T., Wen, G. C., Dai, L. C. & Wang, B. Coal-like material for coal and gas outburst simulation tests. *Int. J. Rock Mech. Min. Sci.* **74**, 151–156 (2015).
23. Verma H. K. et al. Blast induced rock mass damage around tunnels. *Tunn. Undergr. Space Technol.* **71**, 149–158 (2018).
24. Chen, F., Ma, C. D. & Xu, J. C. Dynamic response and failure behavior of rock under static-dynamic loading[J]. *J. Cent. South. Univ. Technol.* **12**(3), 354–358 (2005).
25. Bleier, M. & Nüchter, A. Low-cost 3d laser scanning in air Orwater using self-calibrating structured light. *Int. Archives Photogrammetry Remote Sens. Spat. Inform. Sci.* **42**, 105–112 (2017).
26. Ebrahim, M. A. B. 3D laser scanners' techniques overview. *Int. J. Sci. Res.* **4**(10), 323–331 (2015).
27. Isa, M. A. & Lazoglu, I. Design and analysis of a 3D laser scanner. *Measurement* **111**, 122–133 (2017).
28. Kersten, T. P. & Lindstaedt, M. Geometric accuracy investigations of terrestrial laser scanner systems in the laboratory and in the field. *Appl. Geomatics*. **14**(2), 421–434 (2022).
29. Adebiyet, B., Iliuf, F. A., Orynbassarova, E., Chernov, A. & Idrissov, K. 3D modeling of Satbayev university based on laser scanning and UAV data. *Int. Archives Photogramm. Remote Sens. Spat. Inform. Sci.* **46**, 1–6 (2022).
30. Fahlander, F. & Axelsson, T. The rock, the whole rock, and everything about the rock: 3D-scanning of bronze age rock Art sites in central-eastern Sweden using Leica MS60 and RTC360. *Situ Archaeologica*. **16**, 49–66 (2023).

Author contributions

P.J. and Y.L. were mainly responsible for designing of research methods. P.J. and Y.L. were mainly responsible for writing the entire manuscript. Y.L. were mainly responsible for data collection. P.J. and G.L. were mainly responsible for checking the manuscript. All authors reviewed the manuscript.

Funding

This work was funded by the National Key Research and Development Plan (2022YFC3005703), and the Science and Technology Plan Projects of Hebei Province (23375402D).

Declarations

Competing interests

The authors declare no competing interests.

Additional information

Correspondence and requests for materials should be addressed to Y.L.